ORIGINAL PAPER

High-Temperature Oxidation Behaviours of AlCoCrFeNi High-Entropy Alloy at 1073–1273 K

Jinyang Zhu[1] · Suning Lu[2] · Ying Jin[1] · Lining Xu[2] · Xiuqing Xu[3] ·
Chengxian Yin[3] · Yi Jia[2]

Abstract

The effect of the temperature on the characteristics of the oxide films on AlCoCr-FeNi high-entropy alloy (HEA) at 1073–1273 K was investigated through scanning electron microscopy, energy-dispersive spectroscopy, and x-ray diffraction. Elemental enrichments in the outer oxide layer and internal oxide zone were studied. The oxidation resistance of AlCoCrFeNi HEA was compared with two commercial alloys [825 Ni-based alloy and 2205 duplex stainless steel (DSS)] with similar Cr content at 1273 K. These alloys are ranked as follows in descending order of oxidation resistance at 1273 K: AlCoCrFeNi HEA, 825 Ni-based alloy, and 2205 DSS. At 1273 K, both Cr and Mo were enriched in the outer oxide layer on 825 Ni-based alloy and 2205 DSS. Only Cr enrichment was observed on the AlCoCrFeNi HEA, but the Cr content in the outer oxide layer on the HEA was greater than those on the 825 Ni-based alloy and 2205 DSS. This might be the main reason why the AlCoCr-FeNi HEA showed the best oxidation resistance among the three studied alloys.

Jinyang Zhu and Suning Lu have contributed equally to this work.

✉ Lining Xu
  xulining@ustb.edu.cn

✉ Chengxian Yin
  yincx@cnpc.com.cn

1   National Center for Materials Service Safety, University of Science and Technology Beijing, Beijing 100083, China

2   Corrosion and Protection Center, Institute for Advanced Materials and Technology, University of Science and Technology Beijing, Beijing 100083, China

3   State Key Laboratory of Performance and Structural Safety for Petroleum Tubular Goods and Equipment Materials, CNPC Tubular Goods Research Institute, Xi'an 710077, China

Introduction

Continuing advances are being made in materials science and new materials are being developed. In particular, the development of high-entropy alloy (HEA) extends beyond the traditional alloys. In the 1990s, the HEA was successfully designed for the first time [1, 2]. Early HEAs consisted of five main elements with equal or near-equal molar ratios, and the high mixing entropy served to stabilise these in disordered bulk solid solutions [3–5]. During the past decade, this concept has attracted much attention because it provides a huge opportunity for designing new materials with a variety of excellent properties, such as high strength, high hardness, high wear resistance, and good high-temperature oxidation resistance [3, 6–15]. It is important to study the high-temperature oxidation resistance of HEAs for their potential use in gas turbines, aero engines, and rocket engines. Some studies [12, 16–19] noted that HEAs, similar to traditional alloys, exhibited selective oxidation of alloying elements and that the element Cr could form a uniform and dense Cr_2O_3 oxide film on the surface to improve the high-temperature oxidation resistance. Rao et al. [20] investigated the effect of Al on the high-temperature oxidation resistance of $Al_x Cr_{0.4}CuFe_{0.4}MnNi$ HEAs and discovered that the high-temperature oxidation resistance of the alloys increases with increasing the Al content. Another study [21] reported that the oxide film of Cr–Mn–Fe–Co–Ni HEAs mainly contains Cr and Mn oxides in a 21% O_2 and 79% N_2 atmosphere; moreover, with an increase in temperature (900 °C, 1000 °C, and 1100 °C), the oxide film thickness increases, and oxidation resistance decreases slightly.

The study on high-temperature oxidation behaviours of Ni-based alloys and stainless steels were also becoming a focus in recent research. Romedenne et al. [22] tested the oxidation behaviour of Laser Beam Melted, Electron Beam Melted and wrought Hastelloy X at 950 °C in dry air. The variability of processing parameters and powder compositions strongly impacted the oxidation behaviour. The alloys with high Mn and Si were associated with higher oxidation rates. An et al. [23] tested the high-temperature oxidation resistance of 27Cr1.7Mn9Ni1.5Mo0.3Nb(wt%) duplex stainless steel (DSS) in the temperature range of 900–1100 °C and found that the oxidation rate of DSS increases with temperature. Continuous repairing behaviour was observed as the increased diffused Cr content induced increased ferrite phase transformation.

With regard to the high-temperature oxidation resistance, the characteristics and advantages of HEAs as compared to traditional stainless steels and Ni-based alloys in terms of their composition have not been well investigated. Some studies [23, 24] have reported that for the high-temperature oxidation resistance of Cr-containing alloys, a Cr content > 16% results in the formation of an oxide film mainly comprising of Cr_2O_3 at 900–1100 °C in dry air. Because the high-temperature oxide film of the alloys mainly contains Cr oxide, Cr plays an important role for the high-temperature oxidation performance. Holcomb et al. [25] studied the difference in high-temperature oxidation resistance among CoCrFeMnNi HEA (with Cr content of 22.66%), the Ni-based superalloy 230 (with Cr

content of 22.15%), and the stainless steel 304H (with Cr content of 18.71%) and found that the high-temperature oxidation resistance of the HEA in laboratory air was similar to that of the other two alloys at 650 °C and 750 °C. In the present study, the oxidation behaviour of AlCoCrFeNi HEA at different temperatures (1073–1273 K) was investigated. Furthermore, the difference in high-temperature oxidation resistance among AlCoCrFeNi HEA (with Cr content of 22.36%), the Ni-based alloy 825 (with Cr content of 22.17%), and 2205 DSS (with Cr content of 21.86%) at 1273 K was studied to explore the influence of elemental composition on high-temperature oxidation performance of these alloys. Special attention was paid to the elemental enrichment in different regions in the oxide film.

Materials and Methods

The materials used in the experiment were an AlCoCrFeNi HEA and two commercial corrosion resistant alloys (825 Ni-based alloy, and 2205 DSS). Table 1 displays the elemental composition of the three alloys. The AlCoCrFeNi HEA was made of high-purity (> 99%) Al, Co, Cr, Fe, and Ni and was prepared by arc-melting the elements in a vacuum arc furnace under a high-purity argon atmosphere. To ensure uniform melting of ingredients, the alloy ingot was melted at least five times. The 825 Ni-based alloy and 2205 DSS used in the experiment were two commercial alloys.

The three alloys were cut into cuboid block specimens with dimensions of 10 mm×10 mm×3 mm. The samples were mounted with epoxy resin and then mechanically polished with 400#, 600#, 800#, 1000#, 1500#, 2000#, and 5000# SiC sandpaper. The AlCoCrFeNi HEA and 825 Ni-based alloys were etched in aqua regia (3:1 volume ratio of HCl:HNO$_3$) for 30 s. Furthermore, the 2205 DSS was electrolytically etched in 50% HNO$_3$ solution at 1.2 V for 30 s, washed with clean water, washed with ethanol, and then dried. The microstructure and morphology of the three alloys were assessed using a BX60M Olympus microscopes. Figure 1 shows the micro structure of these three alloys. The AlCoCrFeNi HEA showed a dendritic structure with few grain boundaries. The 2205 DSS had a biphasic microstructure containing austenite and ferrite. The Ni-based alloy mainly consisted of austenite with a few carbides.

Three parallel samples were prepared for each set of oxidation experiments. The samples were ground to 1000# SiC sandpaper, washed with acetone, washed in ethanol with an ultrasonic cleaner for 30 min, and finally dried with cold wind. The size of each sample was accurately measured using a Vernier calliper, and the surface

Table 1 Elemental compositions of AlCoCrFeNi HEA, 825 Ni-based alloy, and 2205 DSS (wt%)

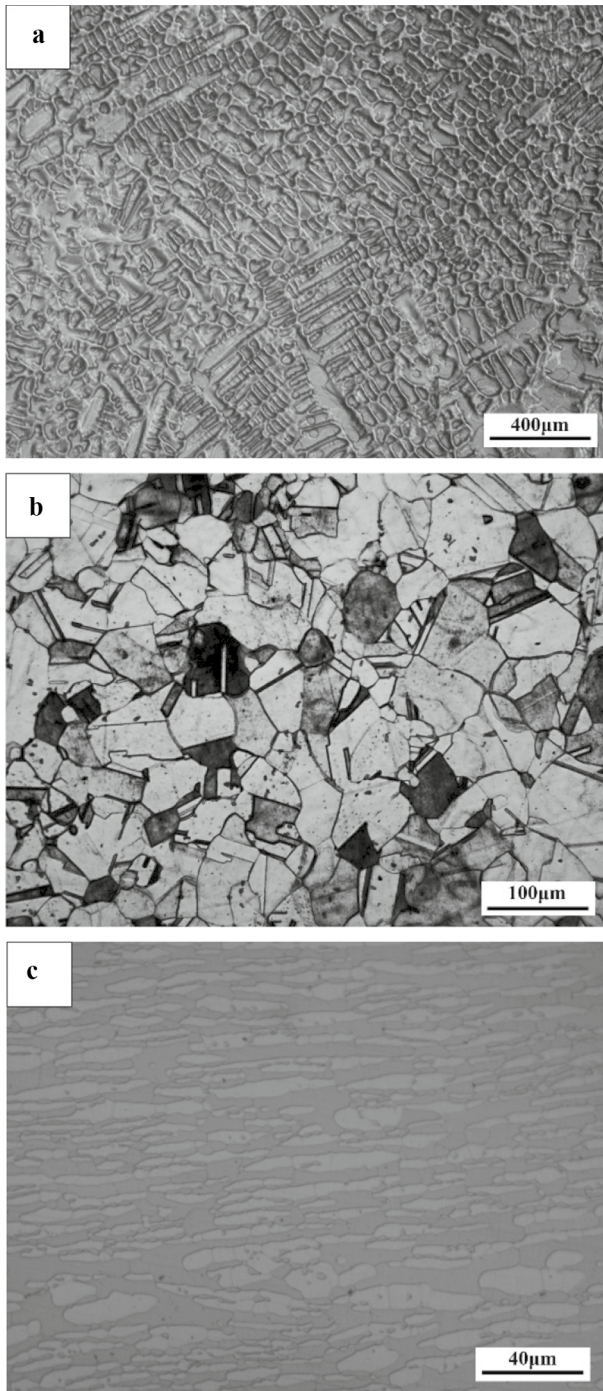| Alloys	Cr	Ni	Fe	Co	Al	Mn	C	Mo	Ti	Si
AlCoCrFeNi HEA	22.36	25.43	25.85	25.12	1.24	–	–	–	–	–
825 Ni-based alloy	22.17	42.37	30.75	–	–	0.93	0.04	2.68	1.06	–
2205 DSS	21.86	5.64	67.93	–	–	1.36	0.03	2.66	–	0.52

Fig. 1 Microstructures of the etched samples for AlCoCrFeNi HEA (**a**), 825 Ni-based alloy (**b**), and 2205 DSS (**c**)

area was calculated. The HEA samples were placed in an SX-G04133 box electric furnace and oxidised at 1073 K, 1173 K, and 1273 K for 100 h. The samples were removed every 10 h, cooled in air, weighed, and then placed back in the furnace for further oxidation. The weight gain data for a given alloy were taken as the average values from three samples. Similarly, the three alloys (the HEA, Ni-based alloy, and DSS) were subjected to an oxidation test at 1273 K for 100 h. The phase composition was characterised by X-ray diffraction (XRD). The microstructure and composition of the oxide films was characterised using a scanning electron microscope (SEM) with energy-dispersive X-ray spectrometry (EDS).

Results and Discussion

Effect of Temperature on the Oxidation Behaviour of the AlCoCrFeNi HEA

Oxidation Kinetics Curves

Figure 2 shows the oxidation kinetics curves of the AlCoCrFeNi HEA during oxidation at different temperatures (1073 K, 1173 K, and 1273 K) for 100 h. Overall, the oxidation resistance of the HEA decreased with an increase in temperature. The mass gain at 1273 K increased rapidly in the first 40 h, and then kept almost steady in the later 60 h. In the early oxidation stage (before 40 h), no film or an incomplete film was formed on the sample surface. The oxidation behaviour was probably controlled by the chemical reaction occurring on the surface. In the later stage, a fully covering and dense oxide film might form and slowed down the continued oxidation of the substrate. The oxidation process was probably controlled by the element
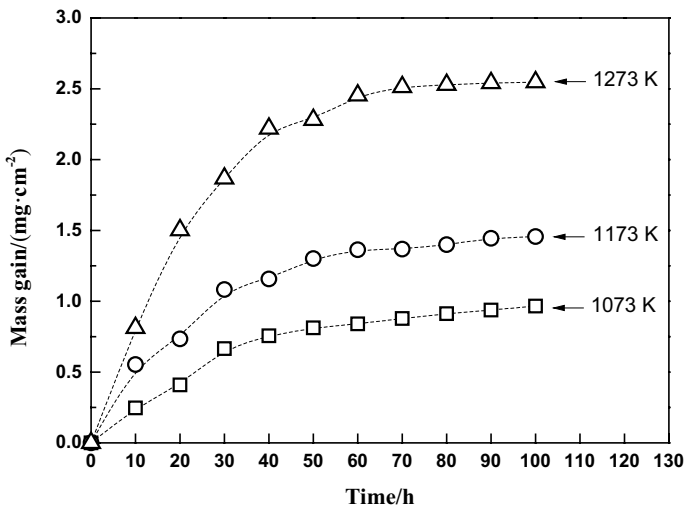
Fig. 2 Oxidation kinetics curves of the AlCoCrFeNi HEA during oxidation at different temperatures (1073–1273 K) for 100 h

diffusion in the oxide film instead of the chemical reaction occurring on the surface, and the oxidation mass gain rate decreased with time dependence of film growth.

Surface Morphologies and XRD Analysis of the Oxide Film on AlCoCrFeNi HEA at Different Temperatures

Figure 3 shows the surface morphologies of the AlCoCrFeNi HEA after oxidation at different temperatures (1073 K, 1173 K, and 1273 K) for 100 h. With increasing
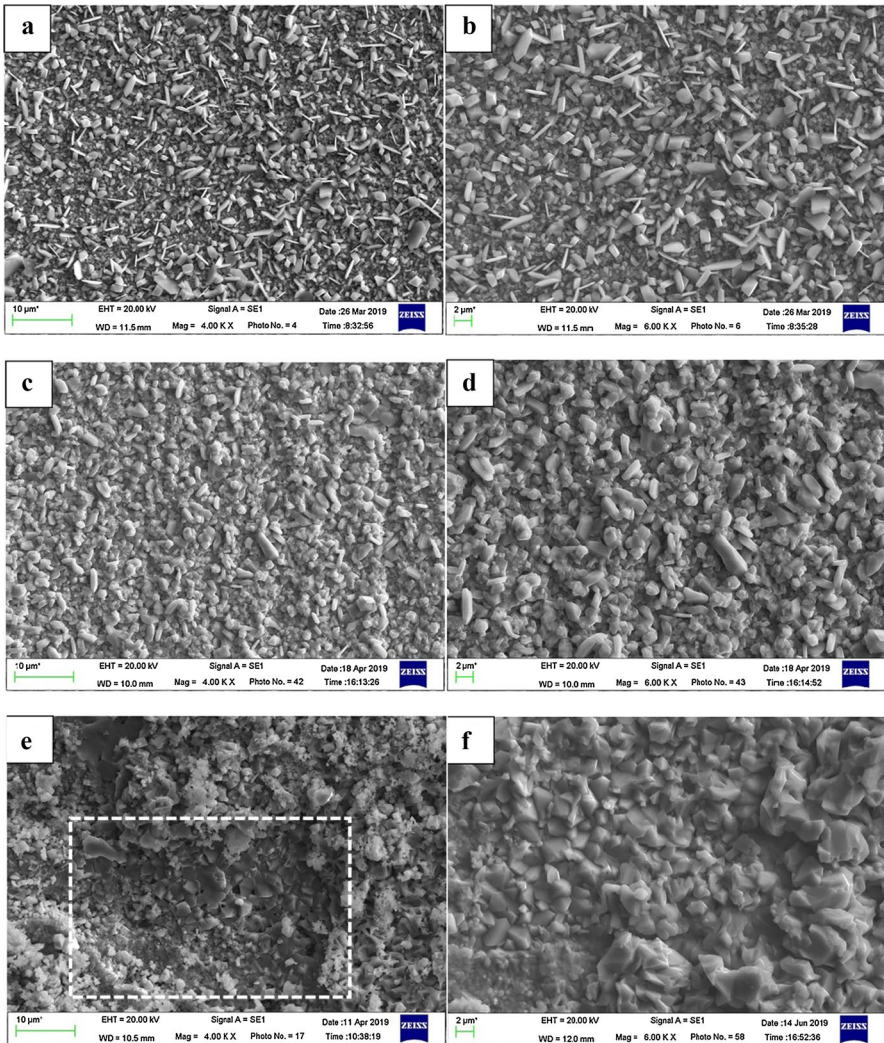

Fig. 3 SEM images of the AlCoCrFeNi HEA after oxidation for 100 h at 1073 K (**a**, **b**), 1173 K (**c**, **d**), and 1273 K (**e**, **f**). The film was uneven and showed a tendency of falling off locally in the white dashed box in (**e**)

temperature, the size of the oxidised particles on the metal surface increased gradually and the surface morphology changed considerably. At 1073 K, the oxide film on the AlCoCrFeNi HEA surface was flat and dense. The corrosion products were flake and block like. At 1173 K, the surface morphology of the oxide film was similar to that at 1073 K except that the oxide particles were slightly larger. When the temperature increased to 1273 K, the oxide film became much looser than those at 1073 K and 1173 K. Furthermore, the film was uneven and it showed a tendency of falling off locally as shown in the white dashed box in Fig. 3e.

Figure 4 presents the phase analysis of the oxide film after oxidation at 1173 K and 1273 K for 100 h. The oxidation products on the AlCoCrFeNi HEA mainly contained Cr_2O_3 and a few $NiFe_2O_4$.

Cross Section Morphologies and Elemental Compositions of the Oxide Film on AlCoCrFeNi HEA at Different Temperatures

To further investigate the characteristics of the oxide film on the AlCoCrFeNi HEA, the cross section morphologies and the chemical composition in different regions of the oxide film after oxidation at different temperatures were studied. Cross section SEM images, and the elemental compositions of the corrosion film on the AlCoCrFeNi HEA after oxidation at different temperatures for 100 h are presented in Figs. 5, 6, and 7.

In Fig. 5, the black and dark grey parts indicate epoxy resin and the outer oxide layer, respectively, and the right side of the outer oxide layer is the internal oxide zone. Overall, the oxide film thickness gradually increased with increasing the temperature. At 1273 K, the film thickness reached about 11 μm, which was much higher than those at 1073 K and 1173 K. At 1073 K, the internal oxide zone had a thickness of
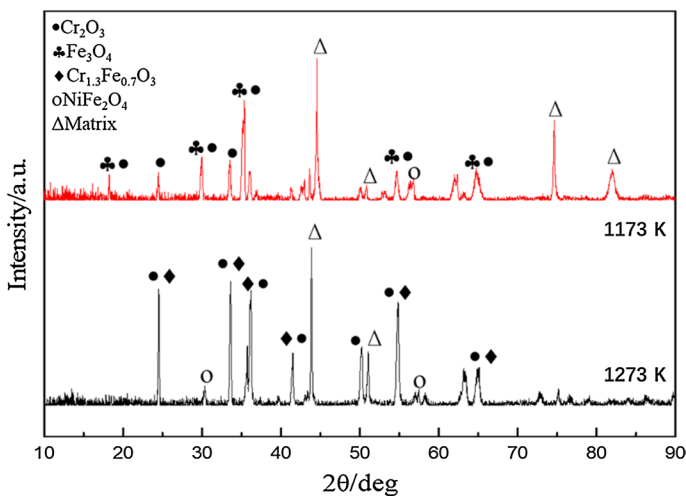

Fig. 4 XRD patterns of the oxide film on the AlCoCrFeNi HEA after oxidation at 1173 K and 1273 K for 100 h
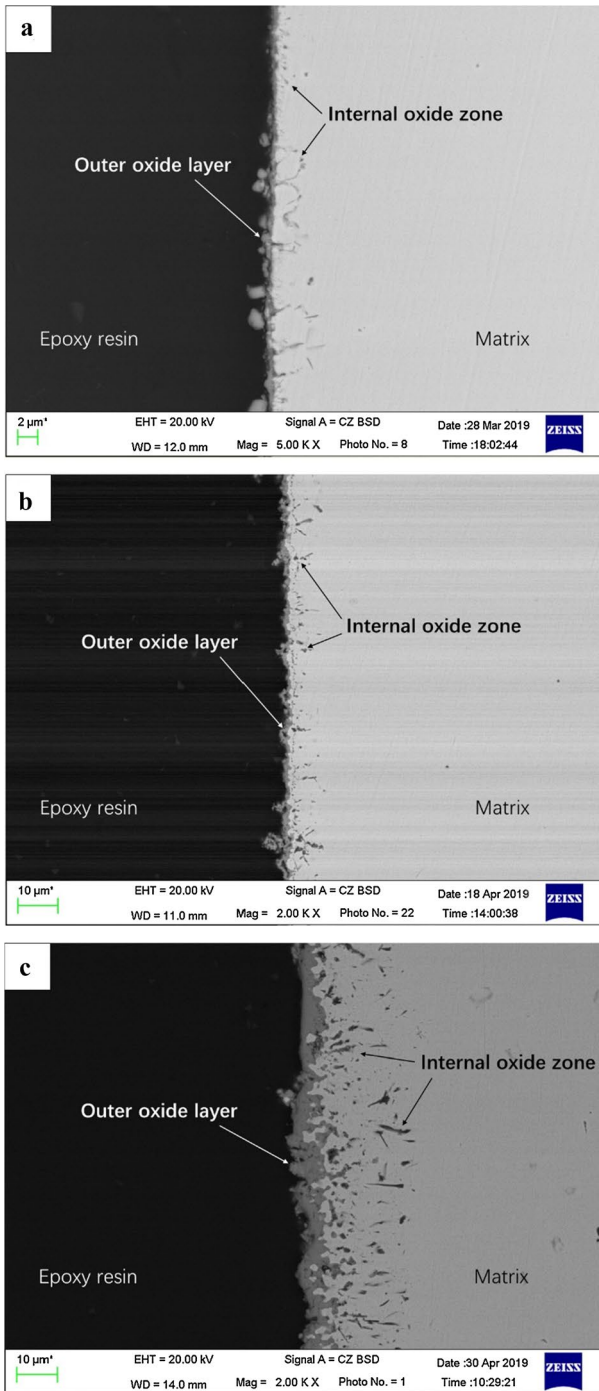
Fig. 5 Cross section morphologies of the AlCoCrFeNi HEA after oxidation for 100 h at 1073 K (**a**), 1173 K (**b**), and 1273 K (**c**)
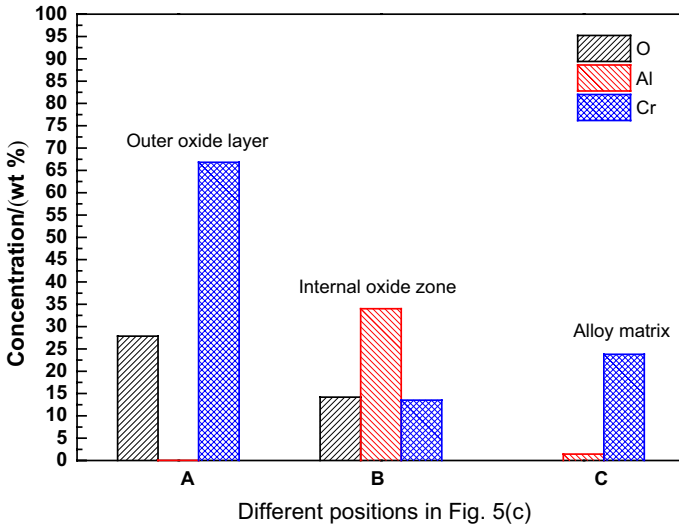
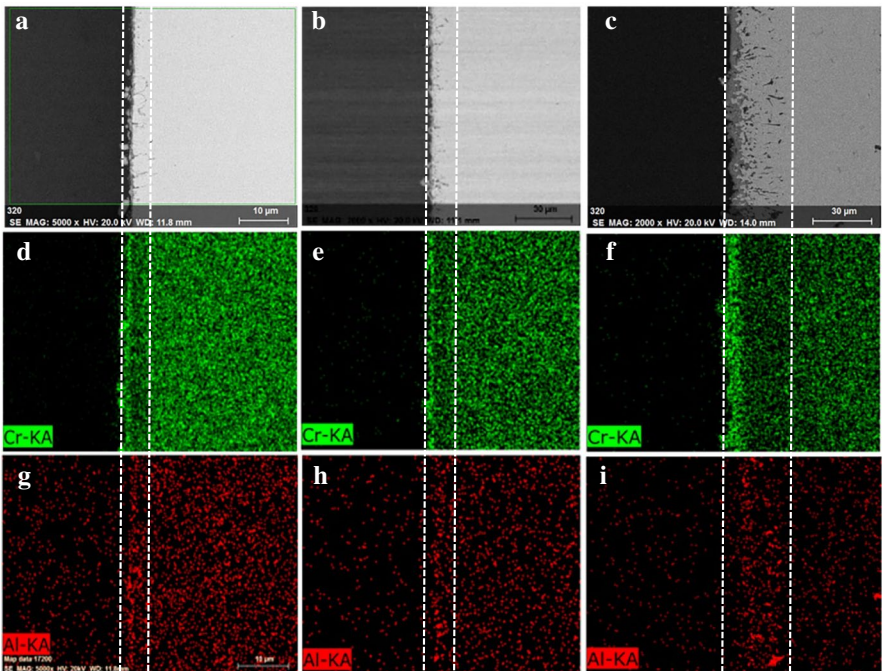**Fig. 6** Elemental content (O, Al, Cr) for different positions in Fig. 5(c)

Fig. 7 EDS maps for the AlCoCrFeNi HEA cross sections after oxidation for 100 h at 1073 K (**a**, **d**, **g**), 1173 K (**b**, **e**, **h**), and 1273 K (**c**, **f**, **i**)

approximately 3 μm. At 1173 K, the internal oxide zone and outer oxide layer were slightly thicker than those at 1073 K. From the colour differences between the internal oxide zone and outer oxide layer, it may be derived that the composition of the inner film should be different form that in the outer film. To confirm this difference, EDS measurements at different regions in Fig. 5c were performed. As shown in Fig. 6, the sum of the Cr and O contents in the outer oxide film was approximately 95%. The O/Cr atomic ratio was approximately 1.36, which approached 1.5, indicating that the presence of Cr_2O_3. The internal oxide zone contained some strip-shaped oxides; these are indicated as black substances in Fig. 5c, and their composition is shown as position B in Fig. 6. A higher Al content (~34%) than that of position C was observed in this area, and the Al/Cr atomic ratio reached about 5.1, which was much higher than that in the alloy matrix (position C) as shown in Fig. 6. This indicated that Al was enriched in the internal oxide zone.

Figure 7 gives the EDS maps for the AlCoCrFeNi HEA cross sections after oxidation at 1073 K (Fig. 7a, d, g), 1173 K (Fig. 7b, e, h), and 1273 K (Fig. 7c, f, i) for 100 h. Overall, in the dashed white line, the Cr was obviously enriched in the outer oxide layer, while Al aggregated in the internal oxide zone. Increasing the temperature only made the oxide film become thicker, but had no obvious effect on the enrichment of Cr and Al in the oxide film on the AlCoCrFeNi HEA. After oxidation at 1273 K, the outer oxide layer exhibited an uniform Cr distribution. A comparison of the cross-sectional morphology (Fig. 7a, b, c) and Al distribution map (Fig. 7g, h, i) indicates that Al is enriched in the dark oxide particles in the internal oxide zone.

Comparison of Oxidation Behaviour Between AlCoCrFeNi HEA, 825 Ni-based Alloy and 2205 DSS at 1273 K

Oxidation Kinetics Curves

Three alloys (AlCoCrFeNi HEA, Ni-based alloy 825, and 2205 DSS) with similar Cr content (~22%) were investigated in this section. The high-temperature oxidation properties of these three alloys were compared in order to discuss the effects of composition on the oxidation performance at 1273 K. Figure 8 presents the oxidation kinetics curves of these three alloys during oxidation at 1273 K for 100 h. The results show that, at 1273 K, the oxidation rate of the AlCoCrFeNi HEA was smaller than those of 825 Ni-based alloy and 2205 DSS. The 2205 DSS exhibited the highest oxidation rate and the mass gain kept increasing with time, whereas the mass gain of 825 Ni-based alloy and AlCoCrFeNi HEA basically kept unchanged after about 60–70 h. This indicated that in addition to the Cr content, other factors also affected the high-temperature oxidation performance. The Fe content of the HEA, Ni-based alloy, and DSS was 25.85%, 30.75%, and 67.93%, respectively. It seems that the lower the Fe content, the better the oxidation performance at 1273 K.
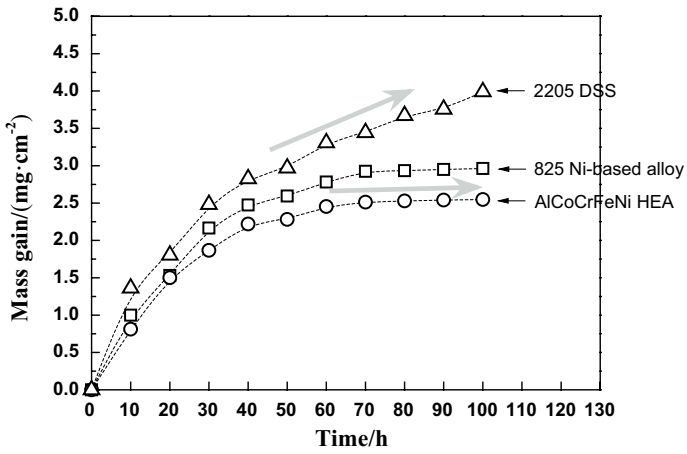
Fig. 8 Oxidation kinetics curves of the AlCoCrFeNi HEA, 825 Ni-based alloy, and 2205 DSS at 1273 K for 100 h
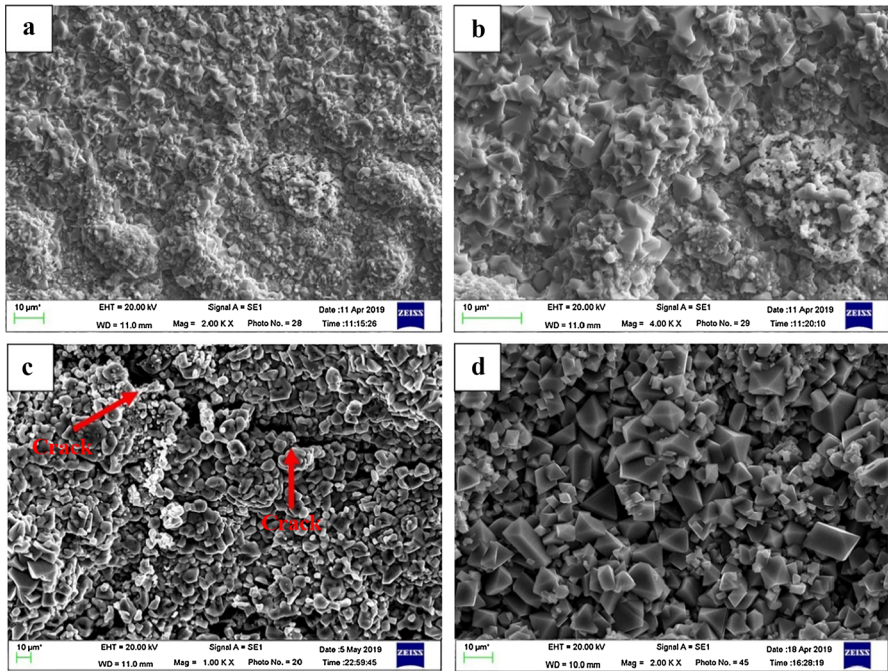

Fig. 9 SEM images of the 825 Ni-based alloy (**a**, **b**) and 2205 DSS (**c**, **d**) after oxidation at 1273 K for 100 h

Surface Morphologies and XRD Analysis of the Oxide Film

Figure 9 shows the surface morphologies of the oxide film on the 825 Ni-based alloy and 2205 DSS formed at 1273 K. Overall, the oxide film on the 825 Ni-based alloy was denser than that on 2205 DSS. The oxide particles on the DSS were bigger than those on the Ni-based alloy. Cracks were visible on the oxide surface of 2205 DSS, as indicated by the red arrows in Fig. 9c. From Fig. 3e, it can be seen that the surface morphology of the oxide film on the AlCoCrFeNi HEA was denser than those on the other two alloys. The oxide particles on the HEA were also the smallest, which indicated the best protectiveness of the oxide film on the AlCoCrFeNi HEA compared to the other two alloys. This is consistent with the oxidation kinetics curves in Fig. 8.

Figure 10 gives the phase analysis of the surface oxides on the 825 Ni-based alloy and 2205 DSS after oxidation at 1273 K for 100 h. As shown in Fig. 10a, the oxidation products in the oxide film on the Ni-based alloy were mainly Cr_2O_3 and some other oxide compounds. For 2205 DSS, the oxidation products in the oxide film were mainly consisted of Cr_2O_3 and $MnCr_2O_4$ or/and Fe_3O_4.

Cross Section Morphologies and EDS Elemental Maps of the Oxide Film

To further investigate the structure and the composition of the oxide film as function of depth, the cross section morphology observations and the EDS maps of the oxide film on the 825 Ni-based alloy and 2205 DSS after oxidation at 1273 K for 100 h were performed and shown in Figs. 11, 12, 13, and 14. The cross-sectional morphology and EDS results of the AlCoCrFeNi HEA under the same condition are given in Figs. 5c, 6 and 7c, f, i.

The cross section morphology observation indicated that the outer oxide layer of the AlCoCrFeNi HEA (Fig. 5c) was the thinnest and that of 2205 DSS (Fig. 11b) was the thickest. Moreover, a small number of pores can be seen in the outer oxide layer on the 2205 DSS, which might reduce the protective property of the oxide film. The EDS tests were performed at different regions on the 825 Ni-based alloy and 2205 DSS. As shown in Figs. 6 and 12, the highest Cr content in the outer oxide layer was observed on the HEA, which reached about 67%. The 2205 DSS showed the lowest Cr content (~50%) among these three alloys. This is consistent with the oxidation resistance as shown in Fig. 9. The surface of the outer oxide layer on the 825 Ni-based alloy contained a small amount of oxide with high Mn content (position A in Fig. 11a). This, along with the XRD data (Fig. 10a), indicated that the outer oxide layer on 825 Ni-based alloy contained Cr-Mn spinel phase. The outer oxide layer on 2205 DSS also contained a certain amount of Mn (position A in Fig. 11b). The Cr and Mn contents in the 825 Ni-based alloy and 2205 DSS were similar. However, the Cr content in the outer oxide layer on 825 Ni-based alloy (~58%) was higher than that on 2205 DSS (~50%); this might be attributable to the lower Fe content in 825 Ni-based alloy than that in 2205 DSS. Dark oxide particles were present in the internal oxide zone of the Ni-based alloy (Fig. 11a). EDS results revealed that the dark oxide particles contained a large amount of Ti (Fig. 13). This, along with the XRD data, indicated that the internal oxide zone of the Ni-based
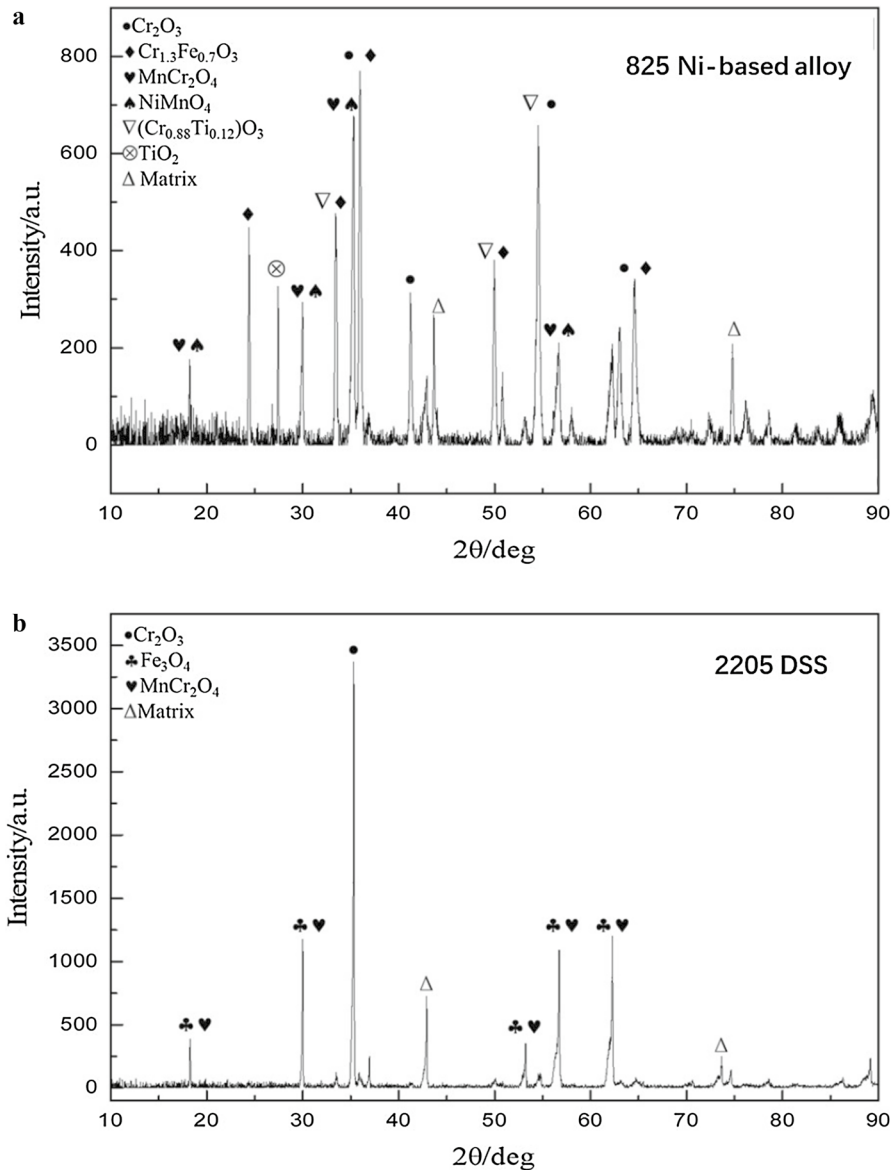
Fig. 10 XRD patterns for 825 Ni-based alloy (**a**) and 2205 DSS (**b**) after oxidation at 1273 K for 100 h

alloy contained TiO_2 or Cr-Ti phase. Dark strip oxide particles were present in the internal oxide zone on 2205 DSS, and EDS results revealed that they contained a large amount of Si. The internal oxide zone on the HEA, as shown in Fig. 5c, contained a few Al-rich strip oxides.

To get a detailed information on the elemental distribution in the oxide film on different alloys, the EDS maps are given in Figs. 13 and 14. From the elemental
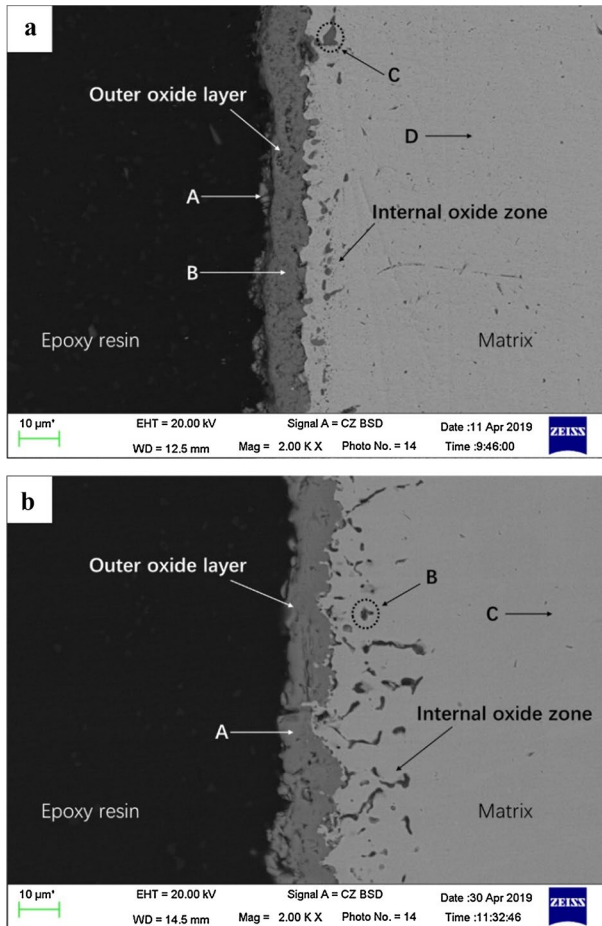
Fig. 11 Cross section morphologies of the 825 Ni-based alloy (**a**) and 2205 DSS (**b**) after oxidation for 100 h at 1273 K

distribution in the area of the white dashed line in Fig. 13, both Cr and Mn were enriched and distributed uniformly in the outer oxide layer on the 825 Ni-based alloy. The element Ti was observed in the internal oxide zone, whose position corresponded to the position of the dark oxide particles in Fig. 11a. Cr and Mn were enriched in the outer oxide layer on the 2205 DSS. However, in addition to the Cr and Mn enrichment, a small amount of Fe was found in the oxide on the 2205 DSS. This is consistent with the EDS result in Fig. 10b. Compared with these two alloys, the AlCoCrFeNi HEA only showed Cr enrichment in the outer oxide layer, but with the highest Cr content (~67%). Moreover, Al was enriched in the internal corrosion zone. These might be the main reasons for the lowest high-temperature oxidation rate of AlCoCrFeNi HEA compared to the other two alloys.
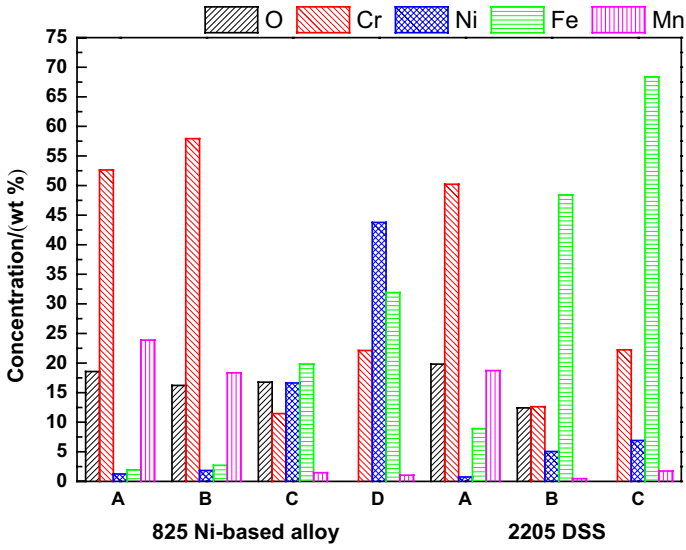
Fig. 12 Elemental content (O, Cr, Ni, Fe, Mn) in the oxide film on the 825 Ni-based alloy (**a**) and 2205 DSS for different positions in Fig. 11
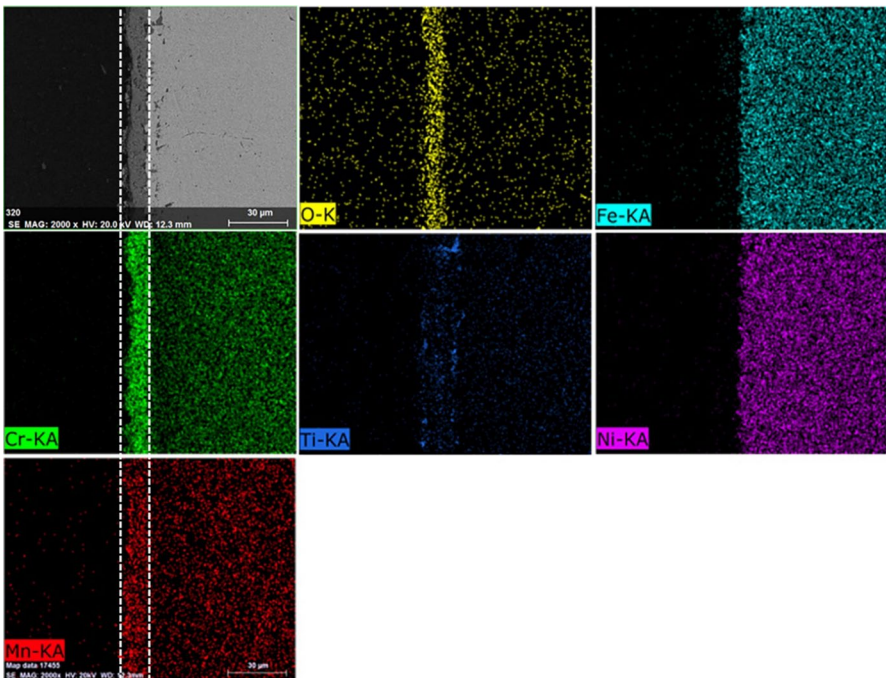

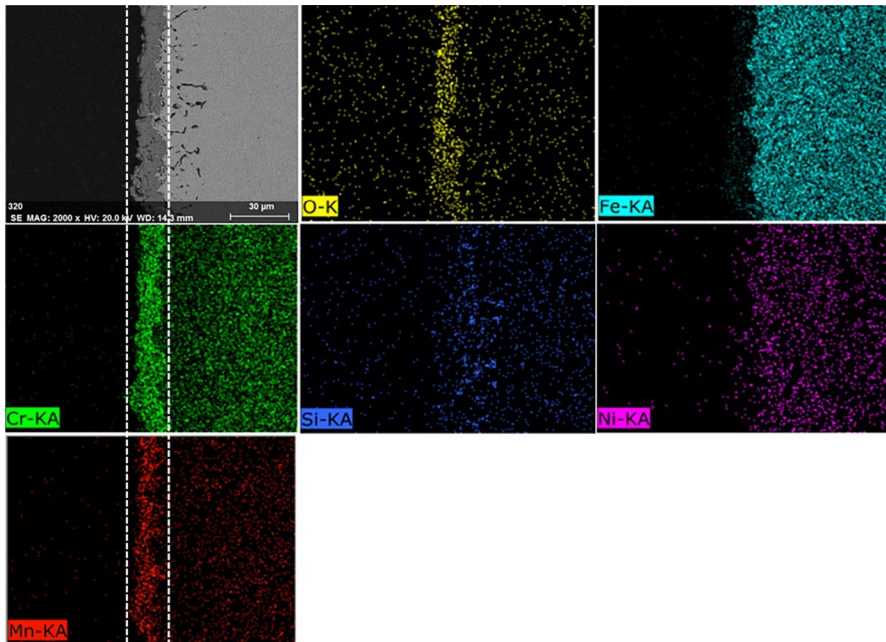**Fig. 13** EDS maps for the 825 Ni-based alloy cross sections after oxidation for 100 h at 1273 K

Fig. 14 EDS maps for the 2205 DSS cross sections after oxidation for 100 h at 1273 K

In summary, the AlCoCrFeNi HEA, 825 Ni-based alloy, and 2205 DSS had a similar Cr content but showed considerably different oxidation resistances at 1273 K (Fig. 8). This is because, as indicated in Figs. 6 and 12, the Cr content in the outer oxide layer ranked as follows in descending order: AlCoCrFeNi HEA, 825 Ni-based alloy, and 2205 DSS. The Cr contents in the matrix are similar among these three alloys, but those in the outer oxide layer are quite different. One of the reasons for this is that both the 825 Ni-based alloy and 2205 DSS contain Mn, and Mn is enriched in the outer oxide layer, making it less rich in Cr.

Conclusions

From the experimental findings on the elemental enrichment in the oxide layer and comparison in the oxidation resistance between the AlCoCrFeNi HEA and two commercial alloys (825 Ni-based alloy and 2205 DSS) with similar Cr content at 1273 K, the high-temperature oxidation behaviour of AlCoCrFeNi HEA was clarified. Specific conclusions are as follows:

1. In the temperature range of 1073–1273 K, the oxidation rate of AlCoCrFeNi HEA decreased with increasing the temperature.
2. The oxidation resistance of the three studied alloys with similar Cr content at 1273 K can be ranked in descending order as the AlCoCrFeNi HEA, 825 Ni-based alloy, and 2205 DSS.

3. Although the three alloys had a similar Cr content in the alloy matrix, the Cr content in the outer oxide layer on the AlCoCrFeNi HEA was much higher than that on the other two alloys. This might be the main reason why the AlCoCrFeNi HEA showed the best oxidation resistance among the three studied alloys.

Data Availability The raw/processed data required to reproduce these findings cannot be shared at this time due to technical or time limitations.

References

1. A. Zhang, J. Han, B. Su and J. Meng, *J. Alloy. Comput.* **725**, 2017 (700).
2. B. Cantor, I. T. H. Chang, P. Knight and A. J. B. Vincent, *Mater. Sci. Eng. A* **375**, 2004 (213).
3. Y. Shi, L. Collins, N. Balke, P. K. Liaw and B. Yang, *Appl. Surf. Sci.* **439**, 2018 (533).
4. H. Luo, Z. Li, A. M. Mingers and D. Raabe, *Corros. Sci.* **134**, 2018 (131).
5. J. Qiu, T. Jin, G. Xiao, Z. Wang, E. Liu and B. Su, *J. Alloys Compd.* **802**, 2019 (93).
6. S. Liu, M. C. Gao, P. K. Liaw and Y. Zhang, *J. Alloys Compd.* **619**, 2015 (610).
7. K.G. Pradeep, Y. Deng, Z. Li, D. Raabe, C.C. Tasan, **534**, 227 (2016).
8. Q. Ye, K. Feng, Z. Li, F. Lu, R. Li and J. Huang, *Appl. Surf. Sci.* **396**, 2017 (1420).
9. H. Zhang, Y. Pan, Y. He and H. Jiao, *Appl. Surf. Sci.* **257**, 2011 (2259).
10. E. P. George, D. Raabe and R. O. Ritchie, *Nat. Rev. Mater.* **4**, 2019 (515).
11. Y. J. Zhou, Y. Zhang, T. N. Kim and G. L. Chen, *Mater. Lett.* **62**, 2008 (2673).
12. W. Kai, C. C. Li, F. P. Cheng, K. P. Chu, R. T. Huang, L. W. Tsay and J. J. Kai, *Corros. Sci.* **121**, 2017 (116).
13. G. Jin, Z. Cai, Y. Guan, X. Cui, Z. Liu, Y. Li and M. Dong, *Appl. Surf. Sci.* **445**, 2018 (113).
14. Y. Y. Chen, U. T. Hong, H. C. Shih, J. W. Yeh and T. Duval, *Corros. Sci.* **47**, 2005 (2679).
15. J. Wu, S. Lin, J. Yeh, S. Chen, Y. Huang and H. Chen, *Wear* **261**, 2006 (513).
16. Y. Liu, C. Cheng, J. Shang, R. Wang, P. Li and J. Zhao, *Trans. Nonferrous Met. Soc. China.* **25**, 2015 (1341).
17. T. M. Butler, J. P. Alfano, R. L. Martens and M. L. Weaver, *JOM.* **67**, 2015 (246).
18. T. M. Butler and M. L. Weaver, *J. Alloys Compd.* **674**, 2016 (229).
19. L. Chen, Z. Zhou, Z. Tan, D. He, K. Bobzin, L. Zhao, K. Tim and M. Ote, *J. Alloys Compd.* **764**, 2018 (845).
20. Z. Rao, X. Wang, Q. Wang, T. Liu, X. Chen, L. Wang and X. Hui, *Adv. Eng. Mater.* **19**, 2017 (1).
21. Y. Kim, Y. Joo, H. S. Kim and K. Lee, *Intermetallics* **98**, 2018 (45).
22. M. Romedenne, R. Pillai, M. Kirka and S. Dryepondt, *Corros. Sci.* **171**, 2020 (108647).
23. L. C. An, J. Cao, T. Zhang and Y. T. Yang, *Mater. Corros.* **68**, 2017 (1116).
24. C. A. Barrett and C. E. Lowell, *Oxid. Met.* **9**, 1975 (307).
25. G. R. Holcomb, J. Tylczak and C. Carney, *JOM.* **67**, 2015 (2326).